Mesoscopic Epifluorescence Tomography: Reconstruction of superficial and deep fluorescence in highly-scattering media

Saskia Björn*, Vasilis Ntziachristos, and Ralf Schulz

Institute for Biological and Medical Imaging (IBMI), Helmholtz Zentrum München, D-85764 Neuherberg, Germany
**saskia.bjoern@helmholtz-muenchen.de*

Abstract: Mesoscopic Epifluorescence Tomography (MEFT) is a technique derived from Laminar Optical Tomography (LOT), determining fluorescence biodistribution by tomographic means in reflectance geometry. A pencil beam is scanned over the region of interest to excite fluorophores hidden within the tissue, while a CCD camera acquires images of reflected fluorescence emissions. This configuration is advantageous whenever transillumination of the specimen is not feasible, e.g., in the presence of skin chambers or when using wavelengths in the visible range where absorption is high. We present simulation and phantom studies recovering deep GFP-like fluorescence in highly scattering and strongly absorbing media with a penetration depth up to 10mm.

OCIS codes: (100.6950) Tomographic image processing; (260.2510) Fluorescence; (290.7050) Turbid media.

References and links

1. V. Ntziachristos, J. Ripoll, L. V. Wang, and R. Weissleder, "Looking and listening to light: the evolution of whole-body photonic imaging," Nat. Biotechnol. **23**(3), 313–320 (2005).
2. D. Hyde, R. de Kleine, S. A. MacLaurin, E. Miller, D. H. Brooks, T. Krucker, and V. Ntziachristos, "Hybrid FMT-CT imaging of amyloid-beta plaques in a murine Alzheimer's disease model," Neuroimage **44**(4), 1304–1311 (2009).
3. N. Deliolanis, T. Lasser, D. Hyde, A. Soubret, J. Ripoll, and V. Ntziachristos, "Free-space fluorescence molecular tomography utilizing 360° geometry projections," Opt. Lett. **32**(4), 382–384 (2007).
4. A. Da Silva, M. Leabad, C. Driol, T. Bordy, M. Debourdeau, J. M. Dinten, P. Peltié, and P. Rizo, "Optical calibration protocol for an x-ray and optical multimodality tomography system dedicated to small-animal examination," Appl. Opt. **48**(10), D151–D162 (2009).
5. D. Kepshire, N. Mincu, M. Hutchins, J. Gruber, H. Dehghani, J. Hypnarowski, F. Leblond, M. Khayat, and B. W. Pogue, "A microcomputed tomography guided fluorescence tomography system for small animal molecular imaging," Rev. Sci. Instrum. **80**(4), 043701 (2009).
6. A. Koenig, L. Hervé, V. Josserand, M. Berger, J. Boutet, A. Da Silva, J. M. Dinten, P. Peltié, J. L. Coll, and P. Rizo, "In vivo mice lung tumor follow-up with fluorescence diffuse optical tomography," J. Biomed. Opt. **13**(1), 011008 (2008).
7. J. Sharpe, U. Ahlgren, P. Perry, B. Hill, A. Ross, J. Hecksher-Sørensen, R. Baldock, and D. Davidson, "Optical projection tomography as a tool for 3D microscopy and gene expression studies," Science **296**(5567), 541–545 (2002).
8. C. Vinegoni, C. Pitsouli, D. Razansky, N. Perrimon, and V. Ntziachristos, "In vivo imaging of Drosophila melanogaster pupae with mesoscopic fluorescence tomography," Nat. Methods **5**(1), 45–47 (2008).
9. E. M. C. Hillman, D. A. Boas, A. M. Dale, and A. K. Dunn, "Laminar optical tomography: demonstration of millimeter-scale depth-resolved imaging in turbid media," Opt. Lett. **29**(14), 1650–1652 (2004).
10. S. Yuan, Q. Li, J. Jiang, A. Cable, and Y. Chen, "Three-dimensional coregistered optical coherence tomography and line-scanning fluorescence laminar optical tomography," Opt. Lett. **34**(11), 1615–1617 (2009).
11. B. Yuan, S. A. Burgess, A. Iranmahboob, M. B. Bouchard, N. Lehrer, C. Bordier, and E. M. C. Hillman, "A system for high-resolution depth-resolved optical imaging of fluorescence and absorption contrast," Rev. Sci. Instrum. **80**(4), 043706–1 (2009).
12. R. Weissleder, and V. Ntziachristos, "Shedding light onto live molecular targets," Nat. Med. **9**(1), 123–128 (2003).

#121136 - $15.00 USD Received 9 Dec 2009; revised 26 Feb 2010; accepted 10 Mar 2010; published 7 Apr 2010

13. A. Garofalakis, G. Zacharakis, H. Meyer, E. N. Economou, C. Mamalaki, J. Papamatheakis, D. Kioussis, V. Ntziachristos, and J. Ripoll, "Three-dimensional in vivo imaging of green fluorescent protein-expressing T cells in mice with noncontact fluorescence molecular tomography," Mol. Imaging **6**(2), 96–107 (2007).
14. R. M. Hoffman, "Recent advances on in vivo Imaging with fluorescent proteins," Fluorescent Proteins, Second Edition **85,** 485–495 (2008).
15. A. Dunn, and D. Boas, "Transport-based image reconstruction in turbid media with small source-detector separations," Opt. Lett. **25**(24), 1777–1779 (2000).
16. S. L. Jacques, and B. W. Pogue, "Tutorial on diffuse light transport," J. Biomed. Opt. **13**(4), 041302 (2008).
17. L.-H. Wang, S. L. Jacques, and L.-Q. Zheng, "MCML--Monte Carlo modeling of light transport in multi-layered tissues," Comput. Methods Programs Biomed. **47**(2), 131–146 (1995).
18. C. C. Paige, and M. A. Saunders, "LSQR: An algorithm for sparse linear equations and sparse least squares," ACM Trans. Math. Softw. **8**(1), 43–71 (1982).

1. Introduction

Fluorescence Tomography is an emerging technique to reconstruct and quantify biofluorescence distributions in tissues or animals, visualizing tissue function at the physiological, metabolical and molecular level with high quantitative accuracy inside living specimen [1]. Tomographic reconstruction typically relies on the inversion of a suitable model for photon propagation. Larger specimens such as mice require a diffusion based model, restricting resolution to the order of 1mm. Here, mostly the near-infrared region of light is used to image probe accumulation in diseases such as Alzheimer's [2] and cancer [3–6].

In smaller specimen, resolution can be greatly improved to an order of 10-50µm using microscopic imaging methods together with alternative mathematical models for light propagation. Two examples are Radon-based methods such as optical projection tomography [7] for transparent specimen or Fokker-Planck [8] for slightly diffusive objects such as drosophila pupae.

All of these methods, however, require transillumination of the specimen and can thus not be applied to larger animals or when skin flaps or skin chambers have to be used. This gap is bridged by methods derived from Laminar Optical Tomography (LOT) which allow for three-dimensional recovery of absorption with approximately 200µm resolution in depths up to a few millimeters [9].

Yuan et al. recently developed a line-scan epifluorescence tomography system and showed the potential to image superficial fluorescence with high sensitivity and penetration depths of up to 2-3mm [10,11]. Similar to this approach we propose a setup for mesoscopic epifluorescence tomography (MEFT) for applications in fluorescent protein imaging in the visible. The system is based on point source illumination instead, and is capable of reconstructing 3D-structures up to 10mm in depth. This depth sensitivity can be achieved even though the fluorescent dyes utilized emit in the visible range where trans-illumination is not practical due to high absorption (in the case of Green Fluorescent Protein (GFP) imaging) or presence of artificial structures such as skin chambers in vivo [12].

Although a few studies for real GFP tomography with fluorescence molecular tomography (FMT) have showcased the principal feasibility [13], the intrinsic brightness of FP expression in vivo [14] allows even for deep-tissue reflectance imaging which has become a standard tool and is much easier to apply. From the development of reflectance-like tomographic approaches such as MEFT we expect an improvement of imaging results without requiring many changes in the experimental protocol.

2. Theory

To model photon propagation in thick turbid media for fluorescence tomography, the diffusion approximation is commonly used. As a diffusion model is only valid far away from the source [15,16], Monte Carlo simulations based on the more accurate radiative transfer equation are used for calculating according sensitivity functions. The Monte Carlo code is based on MCML [17].

#121136 - $15.00 USD Received 9 Dec 2009; revised 26 Feb 2010; accepted 10 Mar 2010; published 7 Apr 2010

In reflectance geometry, unlike transmission geometry, the distance between source and detector points is related to the mean probing depth of the sensitivity functions. In other words, the further away fluorescence emissions are detected from the point of illumination, the deeper on average this signal originated in the tissue (see Fig. 1). In this way, we receive different information for each spot that is scanned and each depends on a differently weighted depth-sensitivity. The detected measurements are then reconstructed with an algorithm that incorporates a corresponding sensitivity matrix **A**.

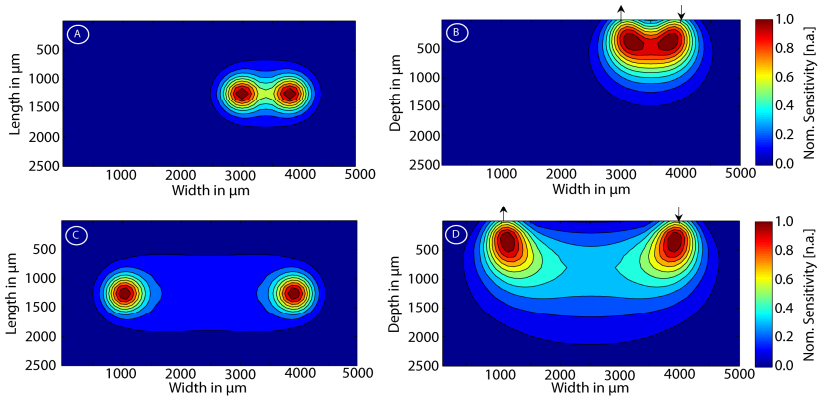

Fig. 1. Exemplary source-detector sensitivity functions as calculated by Monte Carlo simulations (normalized to one, µa = 0.1mm-1, µs = 20mm-1, g = 0.9). A and C indicate the top and B and D the side views of the three dimensional simulated sensitivity functions. As the effective distance between the source (arrow down) and detector (arrow up) increases, the sensitivity profile of the measurements gradually reaches deeper into the medium.

The **A**-matrix is given by a mathematical model of light propagation in scattering tissue and is composed of Green's functions that predict for each voxel the influence of fluorescence on a given source-detector measurement. To model the collimated laser beam used as a source in the experiments, the simulated sensitivity function was convolved with a Gaussian kernel, yielding an accurate description of the source term G^s. For the Green's function of the detector term G^d the sensitivity function was convolved with a window function to model the influence of the rectangular pixel shape on the CCD detector. The specific source-detector sensitivity is then given by the product of G^s and G^d. Figure 1 depicts the accordingly computed Green's functions, showing increasing penetration depth of the sensitivity function for increasing source-detector separations.

The reconstruction problem is given by $y = Ax$, where $y = \{y_{ij}\}$ is the vector of raw MEFT measurements for each source-detector pair ij, and x = $\{x_v\}$ is the 3D volume of fluorescence distribution given for each voxel v. The sensitivity or weight matrix $A = \{A_{ij,v}\}$ is given by source and detector Green's functions as $A_{ij,v} = G^s_{ij,v} \cdot G^d_{ij,v}$.

The necessary inversion of **A** was performed by the iterative LSQR algorithm that has a good numerical stability when **A** is ill-conditioned [18]. The number of iterations was chosen depending on the residual, as described below.

3. Methods and materials

The MEFT system employs a point source to image fluorescence bio-distribution in the visible (Fig. 2). As a light source we utilized a diode laser-pumped all-solid-state laser with an output power of 5mW at a wavelength of λ = 473nm (CNI, Changchun, China). The collimated laser beam was reflected at a dichroic mirror (Thorlabs, Newton, NJ, USA) and scanned over the object's surface using x/z-moving stages (Standa, Vilnius, Lithuania) with a travel range of respectively 25mm in each direction to create arbitrary excitation points. The

#121136 - $15.00 USD Received 9 Dec 2009; revised 26 Feb 2010; accepted 10 Mar 2010; published 7 Apr 2010

emitted light was transmitted back through the dichroic mirror and a long pass colour filter (455nm, Schneider Optik, Bad Kreuznach, Germany). To reduce the intensity of directly reflected light from the external excitation source a linear polarisation filter (ScreenLab, Elmshorn, Germany) was employed. Epi-fluorescence was collected by a 12-bit 3-CCD camera with a frame rate of 51.5Hz (Hamamatsu Photonics, Hamamatsu City, Japan) in the detection pathway of the microscope. The CCD was equipped with an objective that had a focal distance of 35mm (Carl Zeiss, Oberkochen, Germany).

The background levels were subtracted from the images obtained using different source positions in the region of interest and then utilized as input for the reconstruction algorithm described above.

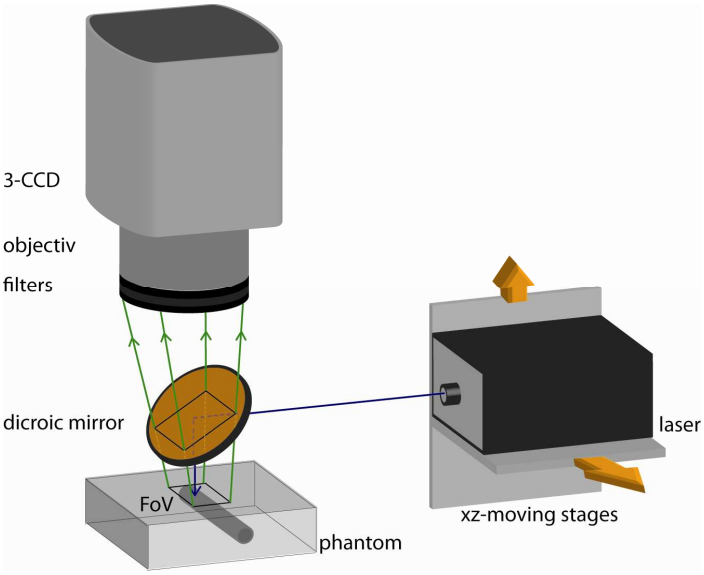

Fig. 2. Schematic setup of the Mesoscopic Epi-Fluorescence Tomography system.

Initial simulation studies were performed to obtain the achievable penetration depth and to approximate the in vivo case of spatially and intensity-wise variable emitter distribution. We simulated for predefined fluorescence test object x_{exact} measurement data y using $y = A \cdot x_{exact} + e_{noise}$. Here the noise term was set at 0.5% additive Gaussian random. Additionally we accounted the dynamic of a 12-bit CCD camera. Reconstructions were performed as described in section 2.

To quantify the theoretically achievable penetration depth, initial simulation studies were performed using six different cylindrical emitters (∅1250µm), containing different amounts of emitter concentration, placed at different depths within a scattering slab (70x35x20mm^3) of tissue-like properties (μ_a = 0.1mm^{-1}, μ_s = 10mm^{-1}, anisotropy factor g = 0.9). A region of interest of the simulation setup is shown in Fig. 3A. A grid of 7x7 source positions at a spacing of 1mm and 700x350 detectors were utilized. Furthermore, we simulated a three-dimensional slab (3x3x2mm^3) of tissue-like properties (μ_a = 0.1mm^{-1}, μ_s = 10mm^{-1}, anisotropy factor g = 0.9) to approximate the in vivo case of spatially and intensity-wise variable emitter distribution. In the tank, we placed two parallel tubes (∅ 150µm) in a distance of 750µm filled with an constantly increasing (Fig. 4Aa) and decreasing (b) fluorescence concentration (c_{low} = 100nM, c_{high} = 1000nM). A grid of 10x10 source positions at a spacing of 1mm and 60x61 detectors were utilized in the simulation.

Initial experimental studies were performed imaging a fluorescent tube (∅ 150µm) inserted in a tank (50x100x50mm^3) filled with intralipid, india ink and water to mimic the

#121136 - $15.00 USD Received 9 Dec 2009; revised 26 Feb 2010; accepted 10 Mar 2010; published 7 Apr 2010

strongly absorbing optical properties of tissue in the wavelength region of GFP emission (μ_a = 0.1mm^{-1}, μ_s = 10mm^{-1}, anisotropy factor g = 0.9). The tube was mounted at different depths in the tank, ranging from 200µm to 10mm. Inside the tube, the scattering and absorbing background media was mixed with a fluorescent dye (3,3′-dioctadecyloxa-carbocyanine perchlorate [DiO], MobiTec, Göttingen, Germany) in a concentration of 200nM. DiO offers excitation and emission wavelengths (λ_x = 489nm, λ_m = 501nm) similar to GFP. Depending on the detected signals exposure times were set between 1ms for a tube depth of 200µm and 4000ms for a tube depth of 10mm. However the exposure time was held constant for all measurements at one tube depth.

A grid of 10x10 source positions separated by 1mm in each direction was used in the imaging experiments. The measured data volume thus consisted of 100 images at 1024 x 1344 pixel resolution. To reduce the data fed into the reconstruction process, images were reduced by a factor of ten using bicubic interpolation, and a region of interest was chosen inside the images. The resulting image pixels were utilized as detector positions in the reconstruction algorithm. The number of iterations ranged between 50 and 100 and were chosen such that the estimated residual $| x'_k - x'_{k+1}| < \tau$, whereas x' is the reconstructed fluorescence bio-distribution, k is the number of iteration and τ is an empirically determined threshold.

The contrast to noise ratio $C = |I_1 - I_2| \cdot \sigma^{-1}$ was calculated to evaluate the signal quality, whereas I_1 and I_2 are the 95th percentile and 5th percentile of the maximum intensity, respectively, and σ is the standard deviation of the dark image noise (see Fig. 6B).

To define system performance, the leakage of excitation light was measured for different exposure times. First, the fluorescent tube was removed and the plain tissue mimicking phantom was excited by the laser. The 95th percentile of the maximum intensity in the accordingly detected raw image was plotted for exposure times ranging from 1ms up to 4200ms (see Fig. 6A)

4. Results

The results of the simulation study that quantifies the achievable penetration depth are shown in Fig. 3. The region of interest of the fluorescent input x_{exact} (A) and reconstructed fluorescence distribution (B) are similar up to a depth of 10mm, while the reconstruction fails to resolve deeper objects. The deviation of the fluorescent input and the reconstructed distribution is illustrated in Fig. 3C.

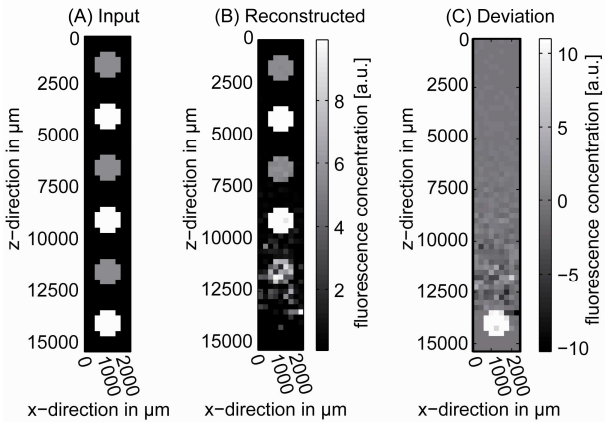

Fig. 3. Simulation of maximum penetration depth. (A) Slice in the region of interest of the simulated slab including six different fluorescent tube emitters at different depths. White emitters contain double the amount of simulated fluorophores. (B) Corresponding slice of the reconstructed fluorescence distribution and (C) deviation of fluorescent input and reconstruction.

#121136 - $15.00 USD Received 9 Dec 2009; revised 26 Feb 2010; accepted 10 Mar 2010; published 7 Apr 2010

The second simulation study demonstrates the potential of the applied LSQR algorithm to reconstruct spatially and intensity-wise variable emitter distributions (Fig. 4). Slices parallel to the surface at the depth of the tubes are shown for the fluorescent input (A) and reconstructed fluorescence distribution (C). Transversal slices through the middle of the tubes are illustrated for the fluorescent input (B) and reconstruction (D). Even though the reconstructed fluorescence distributions seem to be slightly blurred, both, the variable fluorescence concentration and the depth are well reconstructed.

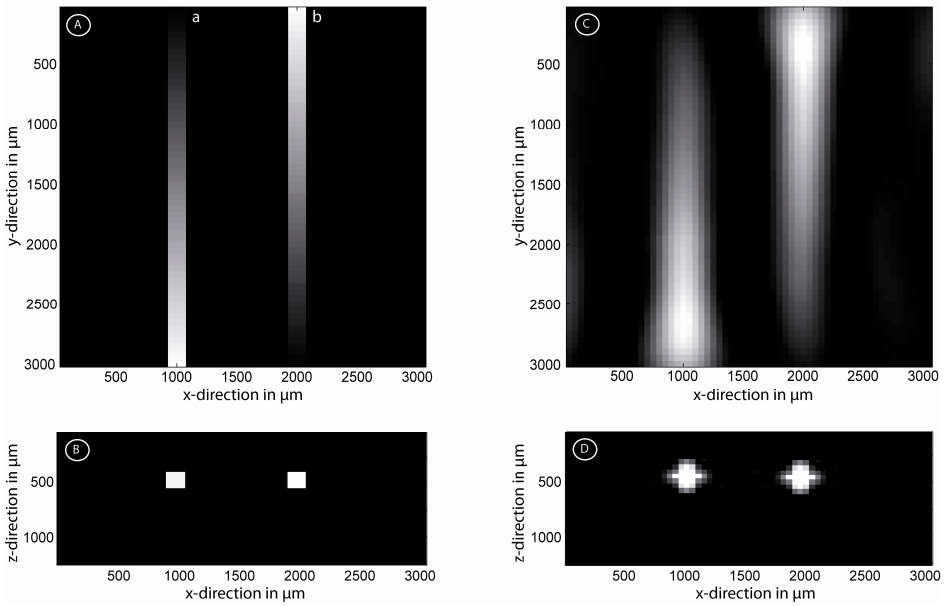

Fig. 4. Demonstration of the LSQR algorithm's potential to reconstruct spatially and intensity-wise variable emitter distributions. Slices parallel to the surface at the depth of the tube for the fluorescent input (A) and reconstructed fluorescence distribution (C). Transversal slices through the middle of the tubes for the fluorescent input (B) and reconstruction (D).

To get an impression of the overall fluorescence intensity distribution within the region of interest, all acquired images (one for each source position chosen) were added together on a per-pixel basis. For the case of the tube being placed at a depth of 200µm this is depicted in Fig. 5A. The according 3D reconstruction of that experiment is partially depicted in Figs. 5B and C, showing recovered axial and transversal slices of the 3D fluorescence distributions at the center of the tube. From these cuts, the full width half maximum (FWHM) of the reconstructed transversal tube shape can be determined in both spatial directions. As expected, there is a clear improvement in specifying the diameter of the tube between the raw (Fig. 5A) and reconstructed (Fig. 5B) data. The raw images appear quite blurred, whereas the reconstructed tube diameter agrees precisely with the actual diameter.

The experiment was repeated with different tube depths. For each experiment, the reconstructed FWHM as well as the recovered location in depth of the tube center was determined. The constant line in Fig. 5D depicts the actual tube diameter, whereas the others depict the size of the FWHM of the intensities in the raw and reconstructed data sets. Due to the highly scattering background the diameter of the tube increases the deeper the tube is hidden in the media. However the reconstructed tube diameter is much closer to the actual value.

The reconstructed tube depths are indicated in Fig. 5E together with the depth as set in the experiment. We found the results to be fairly accurate until a depth of 700µm after which reconstruction accuracy starts to deteriorate.

#121136 - $15.00 USD Received 9 Dec 2009; revised 26 Feb 2010; accepted 10 Mar 2010; published 7 Apr 2010

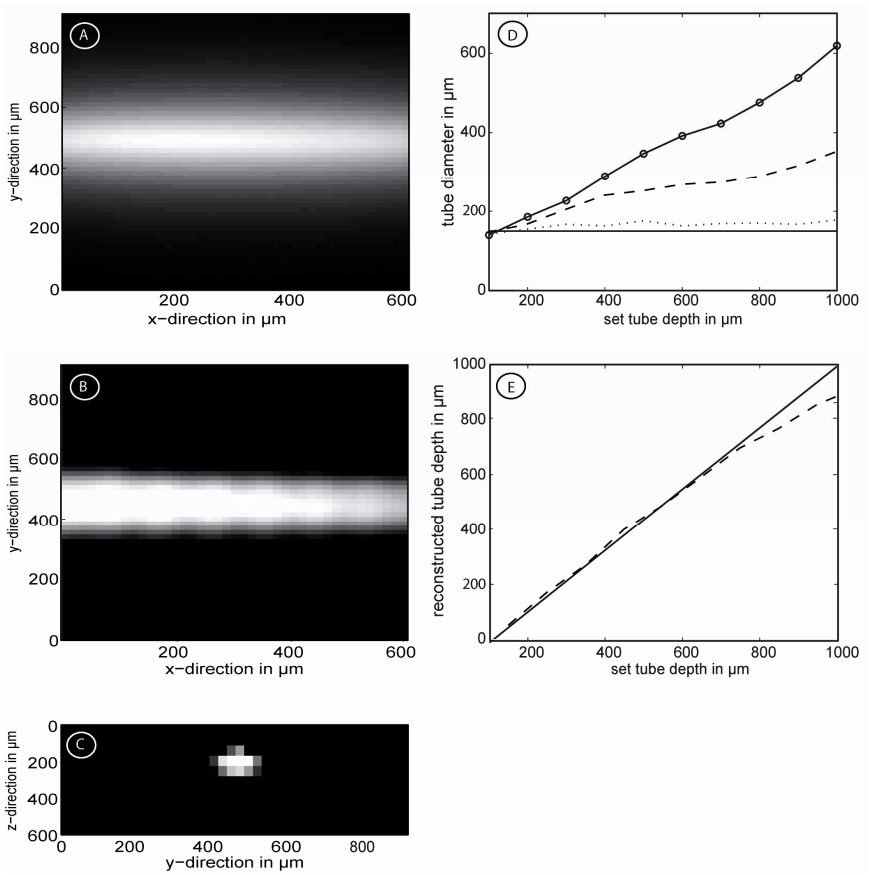

Fig. 5. MEFT phantom imaging results. (A) Summation of all acquired images where the tube centre was located at a depth of 200µm. (B, C) Tomographic slices through the volume of reconstructed fluorescence where the tube was located at a depth of 200µm. (B) A slice parallel to the surface at the depth of the tube. (C) Transversal slice through the reconstructed tube. (D) Plot of the reconstructed tube diameter (FWHM) for different depths of the tube. The constant line depicts the actual tube diameter. The constant line with dots indicates the tube diameter of the raw measurements. The dashed curve shows the reconstructed diameter in y-direction and the dotted in z-direction. (E) Reconstructed depth in comparison to actual depth where the constant line indicates the actual and the dashed curve the reconstructed depths.

The excitation light leakage (A) and the contrast to noise ratio (B) are shown in Fig. 6. We discovered the influence of the leakage to be negligible since it alternates in-between the background levels that are subtracted. As expected the contrast to noise ratio decreases, however also the lower ratio remains sufficiently high for the reconstruction.

#121136 - $15.00 USD Received 9 Dec 2009; revised 26 Feb 2010; accepted 10 Mar 2010; published 7 Apr 2010

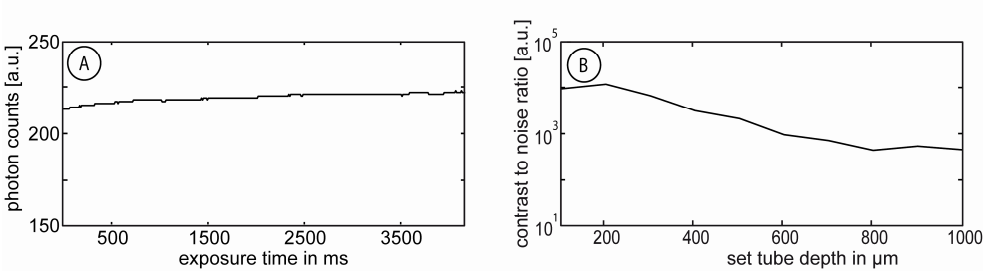

Fig. 6. Characterization of the system performance. (A) Measured leakage of the excitation light as a function of exposure time. (B) Calculated contrast to noise ratio for different tube depths.

5. Discussion

Herein we show the strong potential of our presented MEFT system to reconstruct fluorescence distributions in the visible with a high depth sensitivity and accuracy. In a simulation study taking into account typical noise levels and the limited dynamic range of the camera, a maximum penetration depth of 10mm was estimated. This will, of course, be further limited in practice, due to the presence of optical inhomogeneities, limited laser power, and thus non-optimal illumination of fluorescence images.

Due to the reflectance geometry employed in the setup it is difficult to normalize data using reflectance measurements at the laser wavelengths. As the dynamic range of the overall image is limited, an acquired image of the laser excitation spot would either saturate, or decay rapidly to a background value away from the source spot. This would leave a very small portion of these images to be useful for normalization, thus drastically reduce the maximum source-detector separation and the possible penetration depth. Therefore, to correct for optical inhomogeneities, other potentially novel methods for data preprocessing and preconditioning would be required.

Future work will focus on in vivo measurements, since the microscopic spatial heterogeneities and auto fluorescence cannot be mimicked in tissue phantoms. So far the colour information of the 3CCD camera was not employed and this information could presumably be used for the separation of GFP and auto fluorescence signals in biological specimen.

Acknowledgments

The research described in here was funded by the German Research Council (DFG) under grant number SCHU-2378, and by the German Academic Exchange Service (DAAD) under grant number D/0707645.

#121136 - $15.00 USD Received 9 Dec 2009; revised 26 Feb 2010; accepted 10 Mar 2010; published 7 Apr 2010